Time-lapse full-waveform inversion for elastic TTI media

Yanhua Liu and Ilya Tsvankin
Center for Wave Phenomena, Colorado School of Mines
liuyanhua@mines.edu

ABSTRACT

Time-lapse (4D) full-waveform inversion (FWI) of seismic data can help estimate the subsurface changes due to hydrocarbon production and CO_2 injection. Previously, we have developed a 4D FWI algorithm for VTI (transversely isotropic with a vertical symmetry axis) media. However, the VTI algorithm fails to accurately reconstruct the 4D variations in the presence of dipping anisotropic layers that often cause a tilt of the symmetry axis. Here, we extend the time-lapse FWI methodology to 2D TI media with a tilted symmetry axis (TTI). The symmetry axis is assumed to be orthogonal to the reflectors, so its orientation can be estimated from migrated depth images. The symmetry-axis tilt is incorporated into the modeling code and computation of the FWI gradients by rotating the stiffness tensor using the Bond transformation. The proposed algorithm is tested on the BP TTI model using three different time-lapse strategies. If the 4D data are repeatable, the parameter changes are reconstructed with sufficient accuracy in the presence of moderate noise. We also incorporate the "source-independent" FWI technique to mitigate the influence of errors in the estimated source wavelet and address the wavelet nonrepeatability in time-lapse data. In addition, we discuss the influence of several common nonrepeatability issues on the time-lapse inversion results. Testing on the BP model shows that the parallel-difference time-lapse method is more sensitive to nonrepeatability-related problems than the other employed 4D strategies.

Key words: Time-lapse seismic, full waveform inversion, anisotropy, source-independent, nonrepeatability

1 INTRODUCTION

Time-lapse (4D) seismic processing is an important tool for monitoring subsurface changes caused by hydrocarbon production and CO_2 injection (Lumley, 2010; Smith and Tsvankin, 2013; Pevzner et al., 2017). Full-waveform inversion (FWI) can estimate the medium parameters with high spatial resolution by minimizing the phase and amplitude differences between the observed and simulated data (Vigh et al., 2014; Singh et al., 2018; Zhang and Alkhalifah, 2020; Li et al., 2021b). Therefore, time-lapse FWI, which involves the inversion of the baseline and monitor data, can be efficiently used to monitor 4D changes in the reservoir (Lumley, 2001; Asnaashari et al., 2015; Li et al., 2021a).

Plessix et al. (2010) develop the parallel-difference (PD) 4D FWI strategy that inverts the baseline and monitor data independently using the same initial model. Another workflow (Routh et al., 2012) uses the inversion of the baseline survey to build the initial model for inverting the monitor data (sequential-difference strategy; SD), which improves the convergence of the monitor inversion. To increase the sensitivity of FWI to the changes inside the reservoir, Watanabe et al. (2004) and Denli and Huang (2009) suggest to directly invert the difference between the monitor and baseline data for the time-lapse parameter variations (double-difference strategy; DD). Zhou and Lumley (2021a) average the parameter variations produced by forward (baseline to monitor) and reverse (monitor to baseline) applications of the sequential-difference strategy to reduce the dependence of the estimated time-lapse changes on the accuracy of the inverted baseline model (central-difference strategy; CD). However, the CD approach doubles the computational time compared to the SD and DD methods without a significant improvement in resolution.

Most existing 4D FWI methods are limited to isotropic (often acoustic) media, which limits their applicability. Liu and Tsvankin (2021) extend the methodology of 4D FWI to VTI (transversely isotropic with a vertical symmetry axis) media and

implement it with three different time-lapse strategies mentioned above (PD, SD, and DD). However, transversely isotropic layers (such as shales) may be dipping, which leads to a tilted symmetry axis (e.g., Tsvankin, 2012). For example, uptilted shale layers near salt domes produce an effective tilted TI (TTI) model, often with a large inclination of the symmetry axis.

As shown by a number of synthetic and field-data studies, VTI algorithms become inadequate in the presence of an even moderate symmetry-axis tilt. For example, Behera and Tsvankin (2009) demonstrate that application of VTI velocity-analysis and imaging methods to data from TTI media may lead to significant misfocusing of reflectors and errors in parameter estimation. Wang and Tsvankin (2013) develop 2D P-wave reflection tomography for TTI media and test it on field data from Volve field in the North Sea. Their results show that taking the symmetry-axis tilt into account significantly improves migrated images. Singh et al. (2021) apply an elastic TTI FWI algorithm to the Volve data set and incorporate facies constraints to regularize the inversion. However, to our knowledge, 4D FWI for TTI media has not been discussed in the literature.

The increased number of independent parameters for tilted transverse isotropy makes the objective function more multimodal than that for VTI media, and the model-updating algorithm is more likely to get trapped in local minima. The ill-posedness of FWI can be mitigated by adding regularization terms and prior constraints to the objective function (Asnaashari et al., 2013; Zhang et al., 2018). Another problem is the trade-offs between the TTI parameters that can significantly distort the estimated model. Sensitivity analysis can provide valuable insights into such trade-offs and optimal parameterization for different types of input data (Alkhalifah and Plessix, 2014; Kamath and Tsvankin, 2016; Rusmanugroho et al., 2017; Singh and Tsvankin, 2020).

One of the challenges in FWI is its high sensitivity to the accuracy of the estimated source wavelet (Song et al., 1995; Pratt, 1999; Warner et al., 2013; Luo et al., 2014; Yuan et al., 2014). This issue is particularly significant for time-lapse FWI because the wavelet can change between the baseline and monitor surveys. Liu and Tsvankin (2022) incorporate a source-independent (SI) technique (Choi and Alkhalifah, 2011; Zhang et al., 2016; Bai and Tsvankin, 2019) into 4D FWI for VTI media and demonstrate its effectiveness in mitigating the influence of errors in the source wavelet on the obtained time-lapse parameter variations.

Another common issue in time-lapse seismic is the nonrepeatability (NR) of the baseline and monitor surveys. Ideally, the difference between the monitor and baseline data is caused only by the subsurface changes. However, the data difference can be distorted by a number of other factors. Zhou and Lumley (2021b) discuss the influence of several NR issues on time-lapse parameter inversion and the performance of 4D methods. However, their analysis is limited to isotropic acoustic media with known density, an inadequate model for many case studies.

Here, we extend the previously developed time-lapse VTI FWI algorithm to TTI media, which makes it suitable for a wider range of subsurface models. We begin by discussing FWI methodology for anisotropic media and its application to time-lapse seismic data. Then we introduce a TTI FWI algorithm and implement it using three 4D strategies discussed above (PD, SD, and DD). The proposed methodology is tested on synthetic data for the section of the BP TTI model that includes an anticline. Then the source-independent method is incorporated into the TTI extension of the FWI algorithm to reduce the impact of the distortions in the source signature. In addition, we analyze the influence of several other common nonrepeatability issues on 4D FWI and the performance of the employed time-lapse strategies.

2 INTRODUCTION

Time-lapse (4D) seismic processing is an important tool for monitoring subsurface changes caused by hydrocarbon production and CO_2 injection (Lumley, 2010; Smith and Tsvankin, 2013; Pevzner et al., 2017). Full-waveform inversion (FWI) can estimate the medium parameters with high spatial resolution by minimizing the phase and amplitude differences between the observed and simulated data (Vigh et al., 2014; Singh et al., 2018; Zhang and Alkhalifah, 2020; Li et al., 2021b). Therefore, time-lapse FWI, which involves the inversion of the baseline and monitor data, can be efficiently used to monitor 4D changes in the reservoir (Lumley, 2001; Asnaashari et al., 2015; Li et al., 2021a).

Plessix et al. (2010) develop the parallel-difference (PD) 4D FWI strategy that inverts the baseline and monitor data independently using the same initial model. Another workflow (Routh et al., 2012) uses the inversion of the baseline survey to build the initial model for inverting the monitor data (sequential-difference strategy; SD), which improves the convergence of the monitor inversion. To increase the sensitivity of FWI to the changes inside the reservoir, Watanabe et al. (2004) and Denli and Huang (2009) suggest to directly invert the difference between the monitor and baseline data for the time-lapse parameter variations (double-difference strategy; DD). Zhou and Lumley (2021a) average the parameter variations produced by forward (baseline to monitor) and reverse (monitor to baseline) applications of the sequential-difference strategy to reduce the dependence of the estimated time-lapse changes on the accuracy of the inverted baseline model (central-difference strategy; CD). However, the CD approach doubles the computational time compared to the SD and DD methods without a significant improvement in resolution.

Most existing 4D FWI methods are limited to isotropic (often acoustic) media, which limits their applicability. Liu and Tsvankin (2021) extend the methodology of 4D FWI to VTI (transversely isotropic with a vertical symmetry axis) media and

implement it with three different time-lapse strategies mentioned above (PD, SD, and DD). However, transversely isotropic layers (such as shales) may be dipping, which leads to a tilted symmetry axis (e.g., Tsvankin, 2012). For example, uptilted shale layers near salt domes produce an effective tilted TI (TTI) model, often with a large inclination of the symmetry axis.

As shown by a number of synthetic and field-data studies, VTI algorithms become inadequate in the presence of an even moderate symmetry-axis tilt. For example, Behera and Tsvankin (2009) demonstrate that application of VTI velocity-analysis and imaging methods to data from TTI media may lead to significant misfocusing of reflectors and errors in parameter estimation. Wang and Tsvankin (2013) develop 2D P-wave reflection tomography for TTI media and test it on field data from Volve field in the North Sea. Their results show that taking the symmetry-axis tilt into account significantly improves migrated images. Singh et al. (2021) apply an elastic TTI FWI algorithm to the Volve data set and incorporate facies constraints to regularize the inversion. However, to our knowledge, 4D FWI for TTI media has not been discussed in the literature.

The increased number of independent parameters for tilted transverse isotropy makes the objective function more multimodal than that for VTI media, and the model-updating algorithm is more likely to get trapped in local minima. The ill-posedness of FWI can be mitigated by adding regularization terms and prior constraints to the objective function (Asnaashari et al., 2013; Zhang et al., 2018). Another problem is the trade-offs between the TTI parameters that can significantly distort the estimated model. Sensitivity analysis can provide valuable insights into such trade-offs and optimal parameterization for different types of input data (Alkhalifah and Plessix, 2014; Kamath and Tsvankin, 2016; Rusmanugroho et al., 2017; Singh and Tsvankin, 2020).

One of the challenges in FWI is its high sensitivity to the accuracy of the estimated source wavelet (Song et al., 1995; Pratt, 1999; Warner et al., 2013; Luo et al., 2014; Yuan et al., 2014). This issue is particularly significant for time-lapse FWI because the wavelet can change between the baseline and monitor surveys. Liu and Tsvankin (2022) incorporate a source-independent (SI) technique (Choi and Alkhalifah, 2011; Zhang et al., 2016; Bai and Tsvankin, 2019) into 4D FWI for VTI media and demonstrate its effectiveness in mitigating the influence of errors in the source wavelet on the obtained time-lapse parameter variations.

Another common issue in time-lapse seismic is the nonrepeatability (NR) of the baseline and monitor surveys. Ideally, the difference between the monitor and baseline data is caused only by the subsurface changes. However, the data difference can be distorted by a number of other factors. Zhou and Lumley (2021b) discuss the influence of several NR issues on time-lapse parameter inversion and the performance of 4D methods. However, their analysis is limited to isotropic acoustic media with known density, an inadequate model for many case studies.

Here, we extend the previously developed time-lapse VTI FWI algorithm to TTI media, which makes it suitable for a wider range of subsurface models. We begin by discussing FWI methodology for anisotropic media and its application to time-lapse seismic data. Then we introduce a TTI FWI algorithm and implement it using three 4D strategies discussed above (PD, SD, and DD). The proposed methodology is tested on synthetic data for the section of the BP TTI model that includes an anticline. Then the source-independent method is incorporated into the TTI extension of the FWI algorithm to reduce the impact of the distortions in the source signature. In addition, we analyze the influence of several other common nonrepeatability issues on 4D FWI and the performance of the employed time-lapse strategies.

3 METHODOLOGY OF SOURCE-INDEPENDENT TIME-LAPSE FWI FOR TTI MEDIA

3.1 FWI for anisotropic media

Full-waveform inversion is designed to minimize the difference between the observed and simulated data, typically using the L_2-norm objective function $S(\mathbf{m})$ (e.g., Tarantola, 1984):

$$S(\mathbf{m}) = \frac{1}{2} \left\| \left[\mathbf{d}^{\mathrm{sim}}(\mathbf{m}) - \mathbf{d}^{\mathrm{obs}} \right] \right\|^2, \tag{1}$$

where $\mathbf{d}^{\mathrm{sim}}$ is the data simulated for the model $\mathbf{m}$ and $\mathbf{d}^{\mathrm{obs}}$ is the observed data. Here, we minimize this objective function for multicomponent data from 2D TTI media.

We describe P- and SV-waves in TTI media using a velocity parameterization that was shown to reduce the trade-offs between the TI parameters (Kamath and Tsvankin, 2016). Also, velocities (and their gradients) share the same units, which facilitates the optimization process. This notation includes the P- and S-wave velocities in the symmetry-axis direction ($\mathrm{V_{P0}}$ and $\mathrm{V_{S0}}$), the P-wave velocity in the isotropy plane, which is orthogonal to the symmetry axis ($\mathrm{V_{hor,P}}$), and the P-wave normal-moveout velocity from a horizontal reflector in the corresponding VTI medium ($\mathrm{V_{nmo,P}}$). These four parameters along with density and the symmetry-axis tilt θ fully describe the signatures of P- and SV-waves in the vertical plane that contains the symmetry axis.

Following Kamath and Tsvankin (2016) and Liu and Tsvankin (2021), the adjoint-state method is used to calculate the gradient of the objective function $S(\mathbf{m})$ with respect to the model parameters. We employ a nonlinear conjugate-gradient method to

iteratively update the medium parameters:

$$\frac{\partial S}{\partial \mathbf{m}} = -\Big[\frac{\partial \mathbf{d}^{\rm sim}}{\partial \mathbf{m}}\Big]\,\mathbf{q}\,, \tag{2}$$

where $\mathbf{q}$ is the residual wavefield.

Forward modeling is based on the finite-difference solution of the elastic wave equation for heterogeneous TTI media:

$$\rho\frac{\partial^2 u_i}{\partial t^2} - \frac{\partial}{\partial x_j}\left[c_{ijkl}\frac{\partial u_k}{\partial x_l}\right] = f_i\,, \tag{3}$$

where $\mathbf{u}$ is the particle displacement, ρ is the density, c_{ijkl} is the stiffness tensor, and $\mathbf{f}$ is the density of the body forces. The wave equations for TTI and VTI media are described in more detail in Appendix A.

3.2 Strategies of time-lapse FWI

Time-lapse (4D) FWI operates with the baseline and monitor data sets. Here, we focus on three common 4D FWI strategies discussed in the introduction: the parallel-difference (PD; Plessix et al., 2010), sequential-difference (SD; Asnaashari et al., 2012), and double-difference (DD; Denli and Huang, 2009; Waldhauser and Ellsworth, 2020) methods. To operate directly with the observed $(\mathbf{d}_{\rm m}^{\rm obs} - \mathbf{d}_{\rm b}^{\rm obs})$ and simulated $(\mathbf{d}_{\rm m}^{\rm sim} - \mathbf{d}_{\rm b}^{\rm sim})$ data difference, the DD method generates the "composite" data $\mathbf{d}_{\rm com}$:

$$\triangle\mathbf{d} = (\mathbf{d}_{\rm m}^{\rm obs} - \mathbf{d}_{\rm b}^{\rm obs}) - (\mathbf{d}_{\rm m}^{\rm sim} - \mathbf{d}_{\rm b}^{\rm sim}) = \mathbf{d}_{\rm com} - \mathbf{d}_{\rm m}^{\rm sim}\,, \tag{4}$$

$$\mathbf{d}_{\rm com} = \mathbf{d}_{\rm m}^{\rm obs} - \mathbf{d}_{\rm b}^{\rm obs} + \mathbf{d}_{\rm b}^{\rm sim}\,, \tag{5}$$

where the subscripts "b" and "m" refer to the baseline and monitor data, respectively. The DD method estimates the parameters of the monitor model by minimizing $\triangle\mathbf{d}$ from equation 4; the initial monitor model is obtained by inverting the baseline data.

4 SYNTHETIC EXAMPLE

4.1 2D BP TTI model

The proposed time-lapse FWI algorithm is applied to the section of the 2D BP TTI model (Figure 1a-e), which contains an anticline. The model is 4.5×1.8 km with a grid size of 10×10 m; the data are excited by 56 shots placed at the water surface with a constant interval of 80 m. There are 435 receivers on the sea floor at a depth of 210 m, which emulates ocean-bottom acquisition. The maximum tilt for this section of the BP model does not exceed 35° (Figure 2).

To obtain the initial model (Figures 1f-j), a Gaussian smoothing filter with a standard deviation of 70×70 m is applied to the actual parameter fields. Reflection tomography and/or borehole information can help build the initial model in field-data applications. The monitor model is generated by reducing the baseline parameters $V_{\rm P0}$, $V_{\rm S0}$, and ρ in the target area (the thin horizontal layer) by 10% (Figures 1k, l, and m).

The input data are the vertical and horizontal particle velocities simulated using the elastic wave equation for TTI media. FWI updates all parameters (the velocities and density) simultaneously. A multiscale approach with four frequency bands is implemented to mitigate the cycle-skipping problem in FWI. Data below 2 Hz are excluded from the inversion because such low frequencies are usually unavailable in the field.

To estimate the tilt of the symmetry axis, we conduct depth migration for the initial baseline model and set the axis orthogonal to the reflectors (Wang and Tsvankin, 2013; Singh et al., 2021). Because the tilt for the BP model is mild, we also use a VTI migration code to generate the depth image and estimate the dips, which yields the results that are similar to those for the TTI migration. An alternative way to generate the depth image from the velocity model itself, proposed by Davy et al. (2021), also works well for our model. Because the symmetry-axis tilt is mild and does not change significantly over iterations, we update the tilt only after each inversion stage (frequency band).

As mentioned above, we apply 4D FWI with the parallel-difference (PD), sequential-difference (SD), and double-difference (DD) strategies. The inverted baseline model is applied to the monitor inversion of the SD and DD strategies without any smoothing. For the first test, the monitor data are acquired with perfect repeatability. The results (used below as the benchmark) show that all three strategies reconstruct 4D variations with sufficient spatial resolution (Figure 3). Because of the parameter trade-offs, the time-lapse variations of $V_{\rm hor,P}$ and $V_{\rm nmo,P}$ (which are unchanged) do not completely vanish. The DD strategy reconstructs the 4D variations with the highest resolution and generates the fewest errors outside the reservoir because the inversion of the monitor data operates with the actual 4D data difference. The SD and DD strategies are more computationally efficient and yield fewer artifacts than PD because the monitor inversion starts from the estimated baseline model.

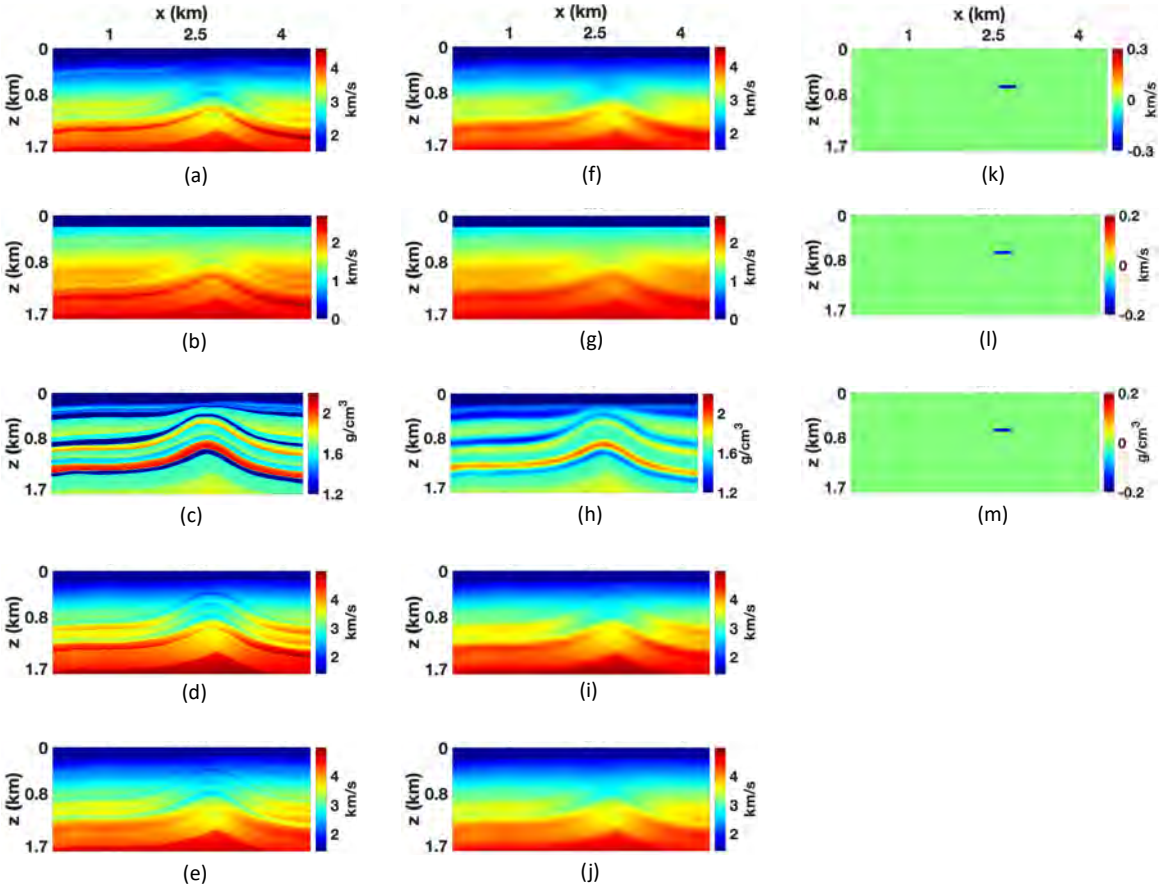

Figure 1. Parameters of the baseline BP TTI model with a grid size of 10×10 m: (a) the P-wave vertical velocity (V_{P0}), (b) the S-wave vertical velocity (V_{S0}), (c) the density (ρ), (d) the P-wave velocity in the isotropy plane ($V_{\mathrm{hor,P}}$), and (e) the P-wave normal-moveout velocity ($V_{\mathrm{nmo,P}}$). The initial baseline model of: (f) V_{P0}, (g) V_{S0}, (h) ρ, (i) $V_{\mathrm{hor,P}}$, and (j) $V_{\mathrm{nmo,P}}$. The actual time-lapse differences in (k) V_{P0}, (l) V_{S0}, and (m) ρ. Note that there are no time-lapse changes in $V_{\mathrm{hor,P}}$ and $V_{\mathrm{nmo,P}}$.

4.1.1 Influence of tilt

To evaluate the influence of the symmetry-axis tilt on the wavefield, we compare the vertical particle velocity for the actual baseline model of V_{P0}, V_{S0}, $V_{\mathrm{hor,P}}$, $V_{\mathrm{nmo,P}}$, and ρ simulated using TTI and VTI algorithms (Figure 4). The reflected, diving, and converted waves computed for the two models match reasonably well for offsets smaller than 2 km because the tilt is relatively mild. The influence of tilt increases with offset x and becomes more significant for waves that cross the dipping flanks of the anticline ($x \geq 2$ km) where the tilt is largest. Because the reservoir is subhorizontal (Figure 2), the VTI algorithm still resolves the parameter changes with acceptable accuracy.

Next, we design a different monitor model where the target layer is dipping and embedded in the left flank of the anticline (Figures 5a-c). After simulating the data for the actual TTI model, we conduct time-lapse FWI using the SD strategy. The 4D TTI algorithm accurately estimates the parameter changes in the reservoir (Figures 5i-m). In contrast, the size and magnitude of the time-lapse parameter variations (especially in ρ) is underestimated if the symmetry-axis tilt is ignored in FWI (Figures 5d-h). In addition, the VTI inversion generates significant false anomalies in all parameters along and below the anticline (red arrows). Evidently, the inadequacy of the VTI model leads to parameter cross-talk that produces false anomalies in the velocities $V_{\mathrm{hor,P}}$ and $V_{\mathrm{nmo,P}}$ (which are held constant). Therefore, it is essential to apply the TTI algorithm if the symmetry axis is tilted inside and around the reservoir, even if the tilt is relatively mild.

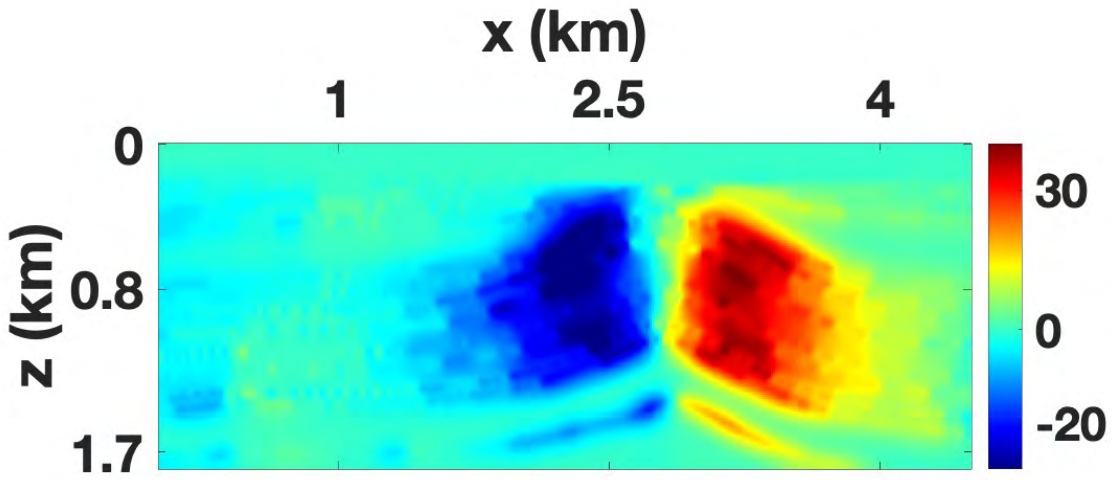

Figure 2. Tilt of the symmetry axis estimated by migrating the baseline data using the actual baseline model.

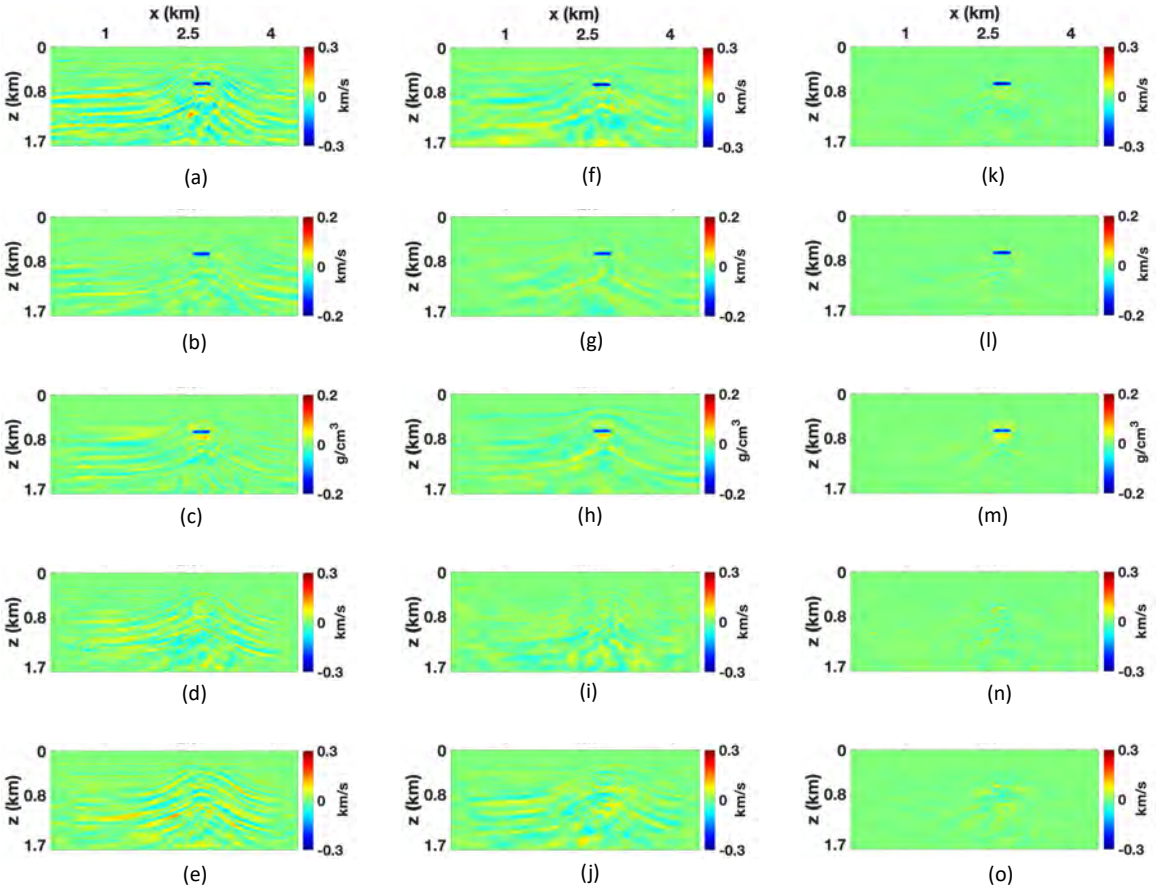

Figure 3. Time-lapse parameter variations obtained from noise-free multicomponent data. The parallel-difference method: (a) V_{P0}, (b) V_{S0}, (c) ρ, (d) $V_{\mathrm{hor,P}}$, and (e) $V_{\mathrm{nmo,P}}$. The sequential-difference method: (f) V_{P0}, (g) V_{S0}, (h) ρ, (i) $V_{\mathrm{hor,P}}$, and (j) $V_{\mathrm{nmo,P}}$. The double-difference method: (k) V_{P0}, (l) V_{S0}, (m) ρ, (n) $V_{\mathrm{hor,P}}$, and (o) $V_{\mathrm{nmo,P}}$.

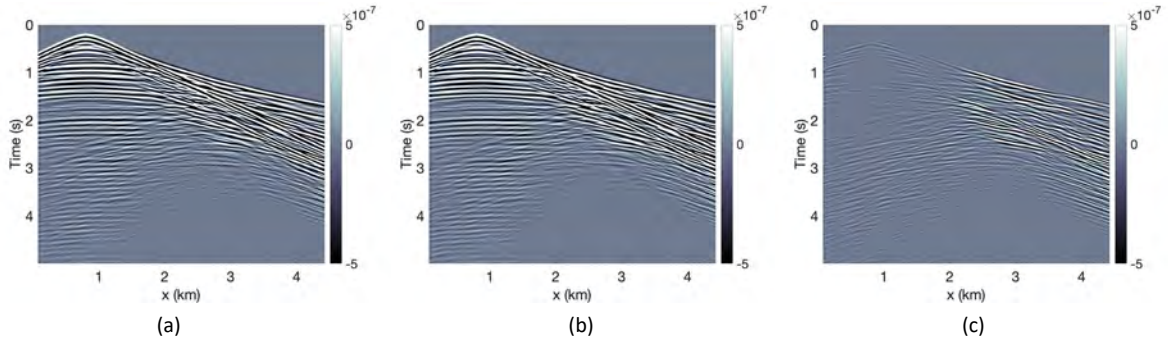

Figure 4. Shot gathers of the vertical particle velocity for: (a) the actual TTI medium, and (b) the corresponding VTI medium. Plot (c) shows the difference between plots (a) and (b).

4.1.2 Influence of nonrepeatable noise

To test the robustness of our TTI method for noisy data, we add nonrepeatable random Gaussian noise with the signal-to-noise ratio (SNR) equal to 15 to both the baseline and monitor data for the model in Figure 1.

Figure 6 shows the inversion results for the parameters V_{P0}, V_{S0}, and ρ. As expected, the added noise degrades the reconstruction of the 4D variations (especially in ρ) and enhances parameter trade-offs. Similar to the noise-free test, the SD and DD strategies produce relatively few artifacts, whereas the noise-induced distortions are more significant in the output of the PD strategy. These observations are consistent with the results of Liu and Tsvankin (2021) for VTI media.

4.1.3 Influence of source wavelet

In 4D seismic processing, the source wavelet is usually estimated from the baseline data after matching monitor and baseline records. However, wavelet extraction is time-consuming and error-prone, and the wavelets for the baseline and monitor data sets may differ. Errors in the wavelet distort the FWI results because they hinder matching of the observed and simulated data.

To analyze the influence of signal distortions, we carry out the inversion using a wavelet (Wavelet 1, Figure 7b) that substantially differs from the actual one (Figure 7a) in both phase and amplitude.

First, we apply FWI to the baseline data using Wavelet 1. Because of the wavelet distortion, the model-updating algorithm could not converge to the global minimum of the objective function and reconstruct the anticline and the reservoir (Figures 8a-c). It is clear that conventional FWI would not be able to estimate the time-lapse changes due to errors in the wavelet.

To reduce the dependence of the inversion results on the accuracy of the source signal, we follow Liu and Tsvankin (2022) and implement the convolution-based source-independent (SI) objective function in the time domain (Choi and Alkhalifah, 2011). The SI algorithm (Figures 8d-f) dramatically improves the accuracy of the inverted parameters and reconstructs the baseline model with a resolution close to that of the benchmark sections (compare Figure 8d-f and Figures 8a-c).

Next we perform the monitor inversion using the source-independent algorithm with the PD and SD strategies and compute the time-lapse parameter variations. The DD method is not employed here because of the phase mismatch between the data simulated for the inverted baseline model using the distorted wavelet and the observed data (Liu and Tsvankin, 2022). Despite underestimating the time-lapse changes inside the reservoir, the output of the PD and SD methods is comparable to the benchmark sections, which is consistent with the results of Liu and Tsvankin (2022) for VTI media. Similar to the benchmark test, the SD workflow recovers the time-lapse changes with a higher resolution and fewer artifacts than the PD strategy (Figure 9). The SI methodology remains sufficiently accurate for noisy data with moderate levels of noise.

4.1.4 Influence of geometry nonrepeatability

The geometries of the baseline and monitor surveys are seldom perfectly repeatable, even if the ocean-bottom nodes (OBN) are equipped with GPS devices. Preprocessing can reduce the impact of the geometry NR but it is difficult to eliminate it completely. To explore the influence of the geometry changes on 4D FWI, we move each source in the monitor survey up and to the right by 10 m. Due to this source displacement, the data difference exhibits changes near and after the first arrival, which are unrelated to the actual time-lapse anomalies (Figure 10b).

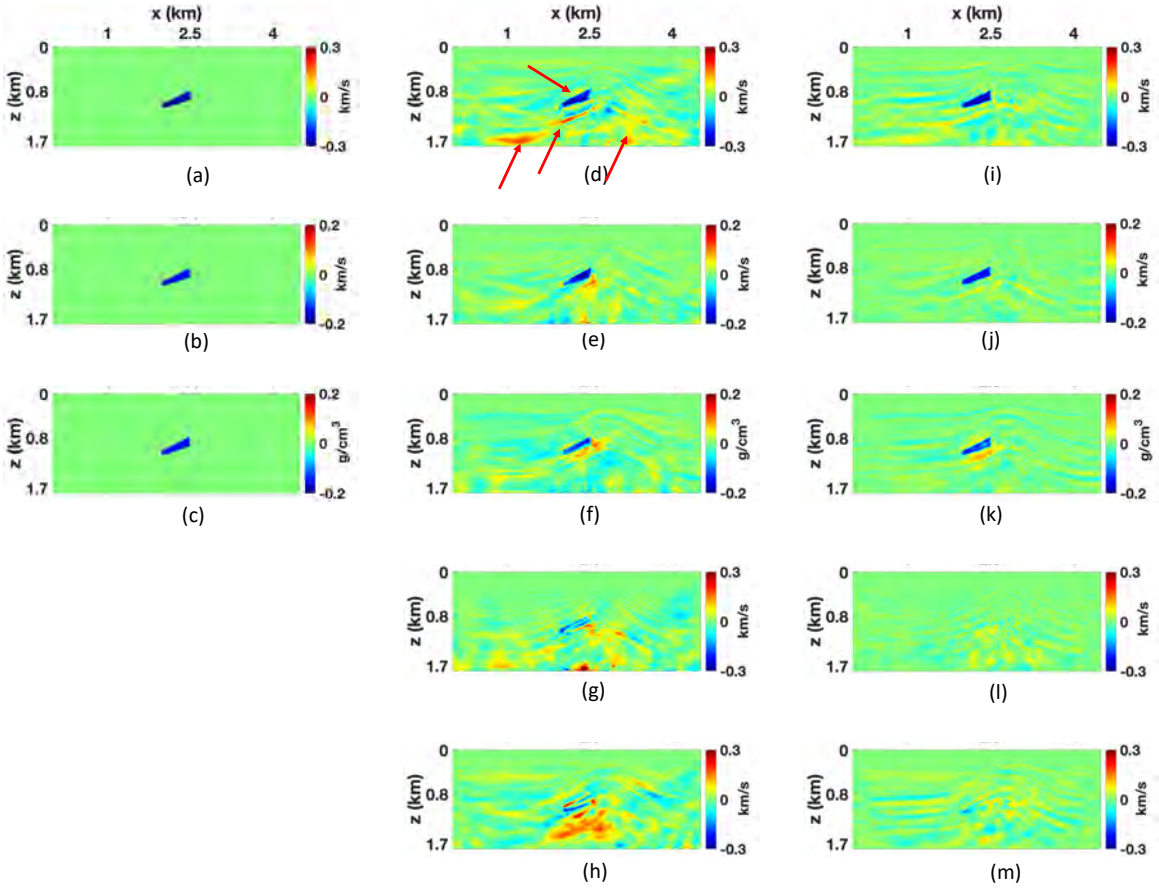

Figure 5. Time-lapse changes inside the reservoir located in a dipping segment of the anticline. The actual time-lapse changes: (a) V_{P0}, (b) V_{S0}, (c) ρ. The time-lapse variations estimated by the VTI [(d) V_{P0}, (e) V_{S0}, (f) ρ, (g) $V_{\mathrm{hor,P}}$, and (h) $V_{\mathrm{nmo,P}}$] and TTI [(i) V_{P0}, (j) V_{S0}, (k) ρ, (l) $V_{\mathrm{hor,P}}$, and (m) $V_{\mathrm{nmo,P}}$] algorithms.

First, 4D FWI is applied using the actual acquisition geometries. Not surprisingly, the shift in the source positions does not significantly influence the reconstruction of the time-lapse changes with all three time-lapse strategies (Figures 11a-c) because the baseline and monitor inversions are performed with the actual geometries. Although the DD strategy operates on the data difference, the error caused by the geometry changes cancels out in equation 4.

Next, to evaluate the influence of geometry errors on the reconstructed 4D parameter changes, the baseline data are inverted using the actual geometry, whereas the monitor inversion is performed with the geometry of the baseline survey. Figures 11d-f show that all three time-lapse strategies produce significant artifacts in the 4D results because of the time shifts between the simulated and observed monitor data caused by the geometry errors. In particularly, these time shifts lead to mispositioning of the reflectors due to the mismatch between these two data sets. Note that the PD strategy starts from a smoothed initial model in the monitor inversion, which gives the model-updating algorithm more flexibility to misplace reflectors. Therefore, the parameter variations produced by the PD strategy (Figure 11d) are distorted more significantly by the geometry error compared to the two other strategies (Figures 11e and f), which agrees with the observation of Zhou and Lumley (2021b).

4.1.5 Influence of water statics

The water velocity may change between the baseline and monitor surveys, and the corresponding time shifts for some deep-water fields can reach 8 ms (Lecerf et al., 2022). Such "water statics" is often corrected by applying time shifts trace-by-trace before the inversion. However, those corrections may not be adequate for time-lapse FWI if the parameter changes are relatively small (Borges et al., 2022). In the next test, we perturb the water velocity of the monitor model to generate time shifts up to 3 ms in the monitor data. Both the baseline and monitor inversions are performed with the water velocity of the baseline model.

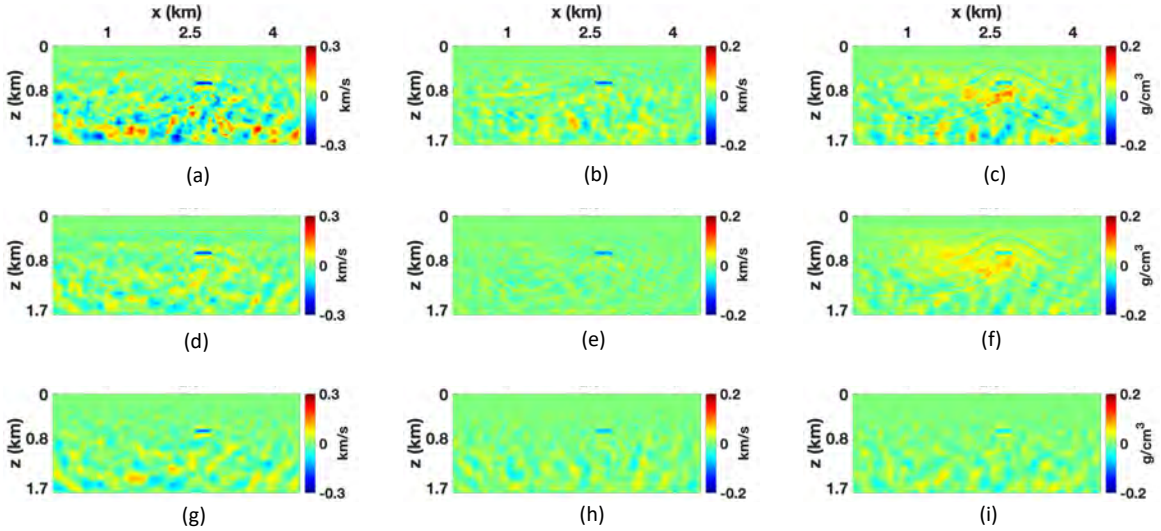

Figure 6. Time-lapse parameter variations obtained from noisy baseline and monitor data (the signal-to-noise ratio is 15) for the model in Figure 1. The parallel-difference strategy: (a) $V_{\rm P0}$, (b) $V_{\rm S0}$, and (c) ρ. The sequential-difference strategy: (d) $V_{\rm P0}$, (e) $V_{\rm S0}$, and (f) ρ. The double-difference strategy: (h) $V_{\rm P0}$, (i) $V_{\rm S0}$, and (j) ρ.

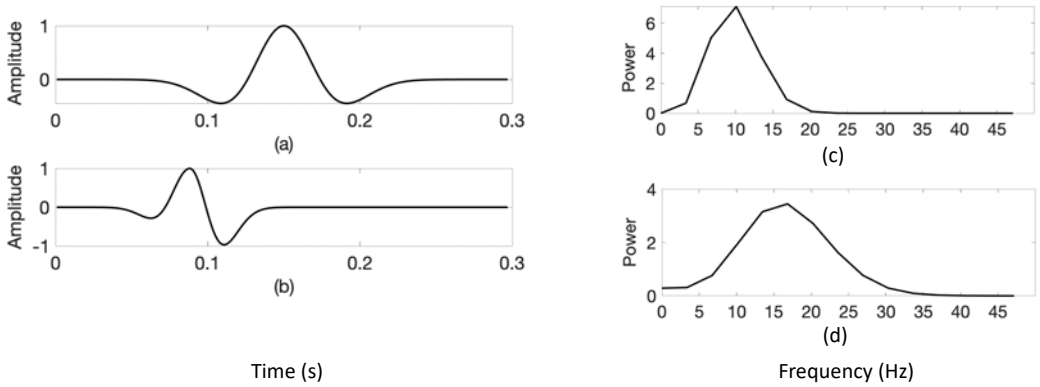

Figure 7. Source wavelets used in the synthetic examples: (a) the Ricker wavelet with a central frequency of 10 Hz (actual wavelet) and (b) the distorted "Ricker" wavelet with a central frequency of 17 Hz (Wavelet 1). The frequency spectra of: (c) the actual wavelet [see plot (a)] and (d) Wavelet 1 [see plot (b)].

Figure 10c shows that the water velocity variations produce noticeable changes in the wavefields above the target area. Because of the incorrect water velocity for the monitor inversion, all three time-lapse strategies generate artifacts and underestimate the size of the reservoir and the amplitude of the parameter changes (Figure 12). Predictably, the parameters $V_{\rm P0}$ and ρ are distorted more than $V_{\rm S0}$ because there are no S-waves in the water. Similar to the geometry NR test above, the PD strategy yields the 4D results with the most artifacts due to the smoothed initial model in the monitor inversion. The SD and DD strategies produce comparable results, which indicates that these two approaches better handle moderate NR-related distortions.

4.1.6 Influence of overburden changes

Hydrocarbon production and CO_2 injection reduce the pore pressure inside the reservoir, which causes stress changes in the surrounding rocks (e.g., Smith and Tsvankin, 2012; Holt et al., 2016). These overburden and underburden changes produce time shifts that can provide useful information for reservoir monitoring (e.g., Smith and Tsvankin, 2013). Precise modeling of stress-

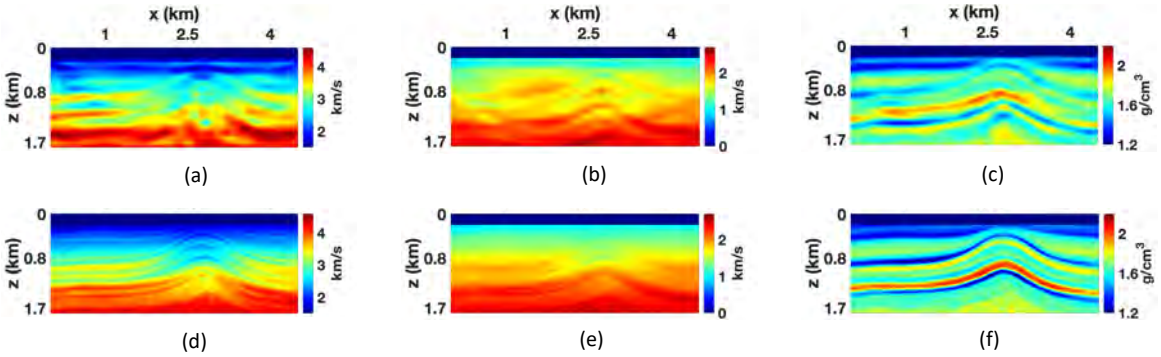

Figure 8. Baseline models estimated using Wavelet 1 by the conventional FWI [(a) V_{P0}, (b) V_{S0}, and (c) ρ] and the source-independent FWI [(d) V_{P0}, (e) V_{S0}, and (f) ρ].

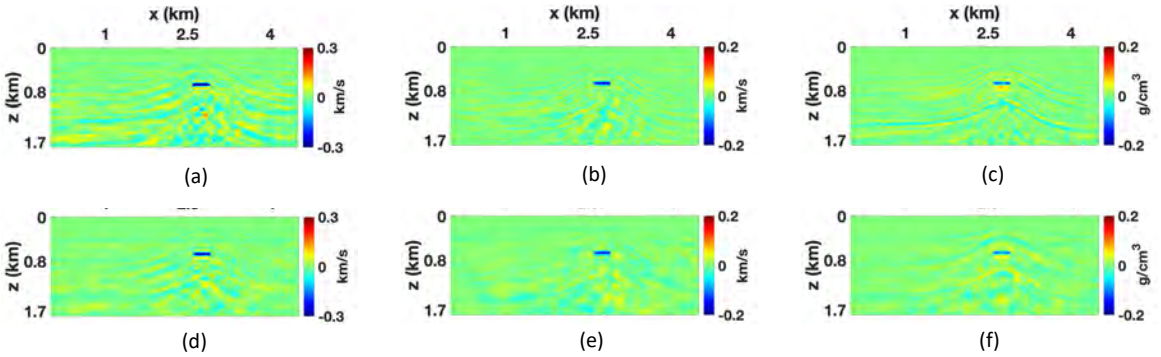

Figure 9. Time-lapse parameter variations reconstructed by the source-independent algorithm using Wavelet 1. The parallel-difference method: (a) V_{P0}, (b) V_{S0}, and (c) ρ. The sequential-difference method: (d) V_{P0}, (e) V_{S0}, and (f) ρ.

related velocity variations is beyond the scope of this paper, so here we simulate such overburden changes by simply increasing the baseline velocities V_{P0} and V_{S0} above the reservoir by up to 4% for the monitor survey (Figures 13a and b).

The influence of the overburden changes is visible in the difference between the monitor and baseline data (Figure 10d). Still, likely because the amplitude of the overburden velocity changes is smaller than those in the reservoir, all three strategies are able to reconstruct the time-lapse variations in the reservoir and overburden with sufficient accuracy (Figure 13). Indeed, FWI is generally capable of estimating the entire model, although relatively large overburden anomalies could potentially mask those in the reservoir. Similar to the repeatability tests above, the DD strategy (Figures 13g and h) reconstructs the parameter changes with the highest resolution and fewest artifacts. This test also illustrates the sensitivity of our algorithm to relatively small changes in the overburden for input data with a low noise level.

5 CONCLUSIONS

We extended the previously developed 4D FWI methodology from VTI to TTI media, which makes it suitable for a wide range of subsurface structures. The algorithm is tested on the anticlinal section of the BP TTI model using three difference time-lapse strategies: the parallel- (PD), sequential- (SD), and double-difference (DD) workflows. To mitigate cycle-skipping, a multiscale technique with four frequency bands is employed in both the baseline and monitor inversions. The velocity parameters responsible for P- and SV-wave propagation in TTI models are updated (along with density) simultaneously at each iteration. The tilt of the symmetry axis is estimated from the structure dips by setting the axis orthogonal to reflectors in migrated images. The tilt model is updated after completing the inversion for each frequency band. If the baseline and monitor data are repeatable, our algorithm reconstructs the time-lapse variations of the TTI parameters with high spatial resolution, even in the presence of moderate noise.

We also incorporated the source-independent (SI) technique into FWI to mitigate the influence of errors in the estimated source

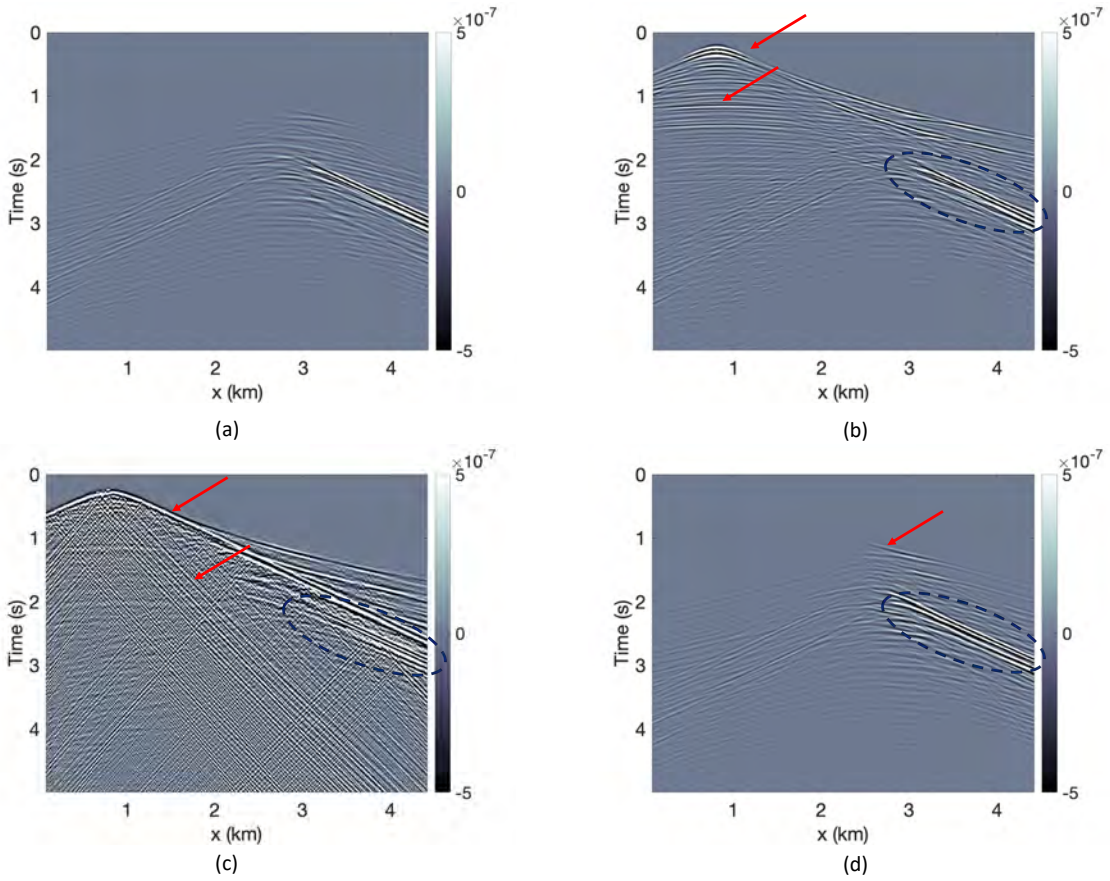

Figure 10. Difference between the vertical particle-velocity components from the monitor and baseline surveys: (a) the perfectly repeatable data (referred to as the actual difference) and the data with (b) geometry nonrepeatability, (c) water statics, and (d) overburden changes. The actual differences caused by the reservoir changes are circled in blue. The noise caused by nonrepeatability is marked by the red arrows.

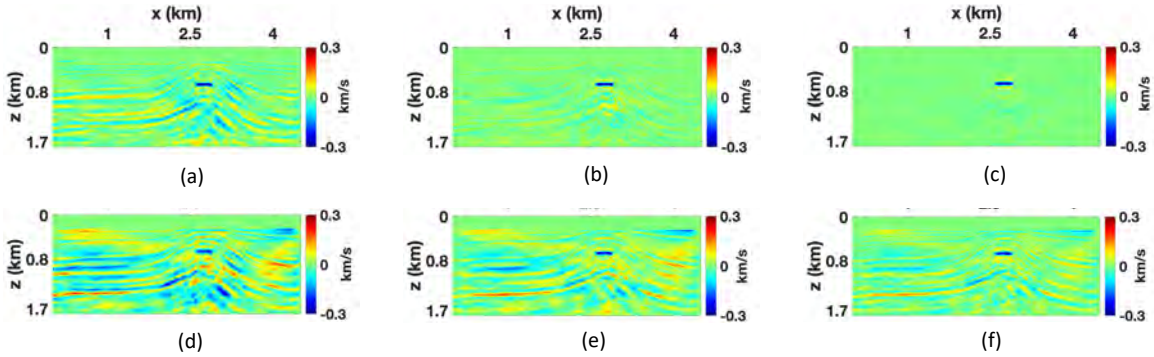

Figure 11. Time-lapse parameter variations of the velocity $V_{\mathrm{P}0}$ estimated from the data with geometry nonrepeatability. The results obtained with the actual acquisition geometries: (a) the parallel-difference method, (b) the sequential-difference method, and (c) the double-difference method. The results obtained using the baseline geometry in the inversion of both the baseline and monitor data: (d) the parallel-difference method, (e) the sequential-difference method, and (f) the double-difference method.

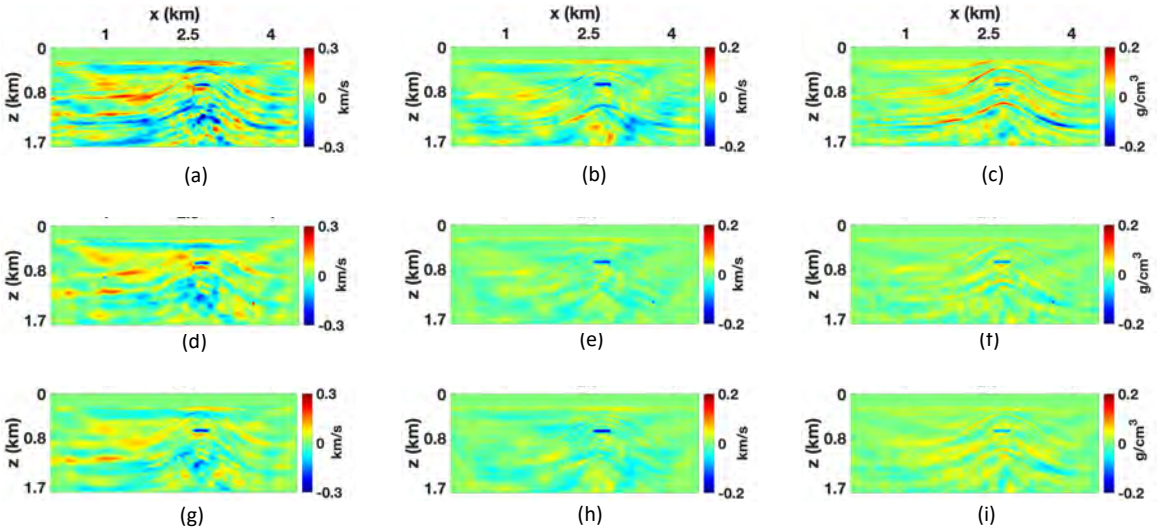

Figure 12. Time-lapse parameter variations estimated from the data with "water statics." The parallel-difference method: (a) V_{P0}, (b) V_{S0}, and (c) ρ. The sequential-difference method: (d) V_{P0}, (e) V_{S0}, and (f) ρ. The double-difference method: (g) V_{P0}, (h) V_{S0}, and (i) ρ.

wavelet on the time-lapse results. The SI FWI algorithm proved capable of reconstructing 4D parameter changes with sufficient accuracy even for a strongly distorted wavelet and noisy data. Employed with the parallel-difference and sequential-difference strategies, the SI FWI algorithm can overcome the source-wavelet nonrepeatability (NR) issue in field-data applications.

In addition, we analyzed the impact of other common NR problems, such as geometry changes, water statics, and time-lapse velocity variations in the overburden. In the test with different source locations for the baseline and monitor surveys, the time-lapse FWI that operated with the actual acquisition geometries accurately estimated the 4D changes. Water statics was shown not to have a significant influence on the inverted parameter variations, unless the corresponding time shifts are comparable to those caused by the reservoir changes. If stress-induced velocity changes in the overburden do not dominate the time-lapse response, FWI is capable of resolving the 4D parameter variations in the entire model including the reservoir.

Our testing also demonstrates that NR issues are best handled with the SD and DD strategies, whereas the results obtained with the PD workflow are generally inferior. The PD strategy operates with a smoothed initial model, for which the NR-induced time shifts between the simulated and observed data may lead to significant distortions, such as reflector mispositioning. The SD and DD strategies generally produce comparable 4D results, with the latter reconstructing the time-lapse changes with the fewer artifacts for data with a low level of noise and high repeatability. Note that the performance of the SD and DD strategies may vary with the model structure, the size of the reservoir, and the amplitude of the time-lapse changes. Therefore, in field applications, it is advisable to test both strategies on a subset of the data prior to processing the entire survey.

6 ACKNOWLEDGMENTS

We thank the members of the Anisotropy-Team at the Center for Wave Phenomena (CWP) in the Geophysics Department at Colorado School of Mines for useful discussions. This work is supported by a joint project with INPEX and the Consortium Project on Seismic Inverse Methods for Complex Structures at CWP.

7 APPENDIX A

8 WAVE PROPAGATION IN 2D TILTED TI MEDIA

We consider a TTI medium with the symmetry axis confined to the $[x, z]$-plane of a Cartesian coordinate system. The $[x, z]$-plane is also assumed to coincide with the dip plane of the subsurface structures to make wave propagation two-dimensional. The wave equation for P- and SV-waves in such 2D TTI media can be written as:

$$\rho \frac{\partial v_x}{\partial t} = \frac{\partial \sigma_{xx}}{\partial x} + \frac{\partial \sigma_{xz}}{\partial z} + f_x, \tag{A-1}$$

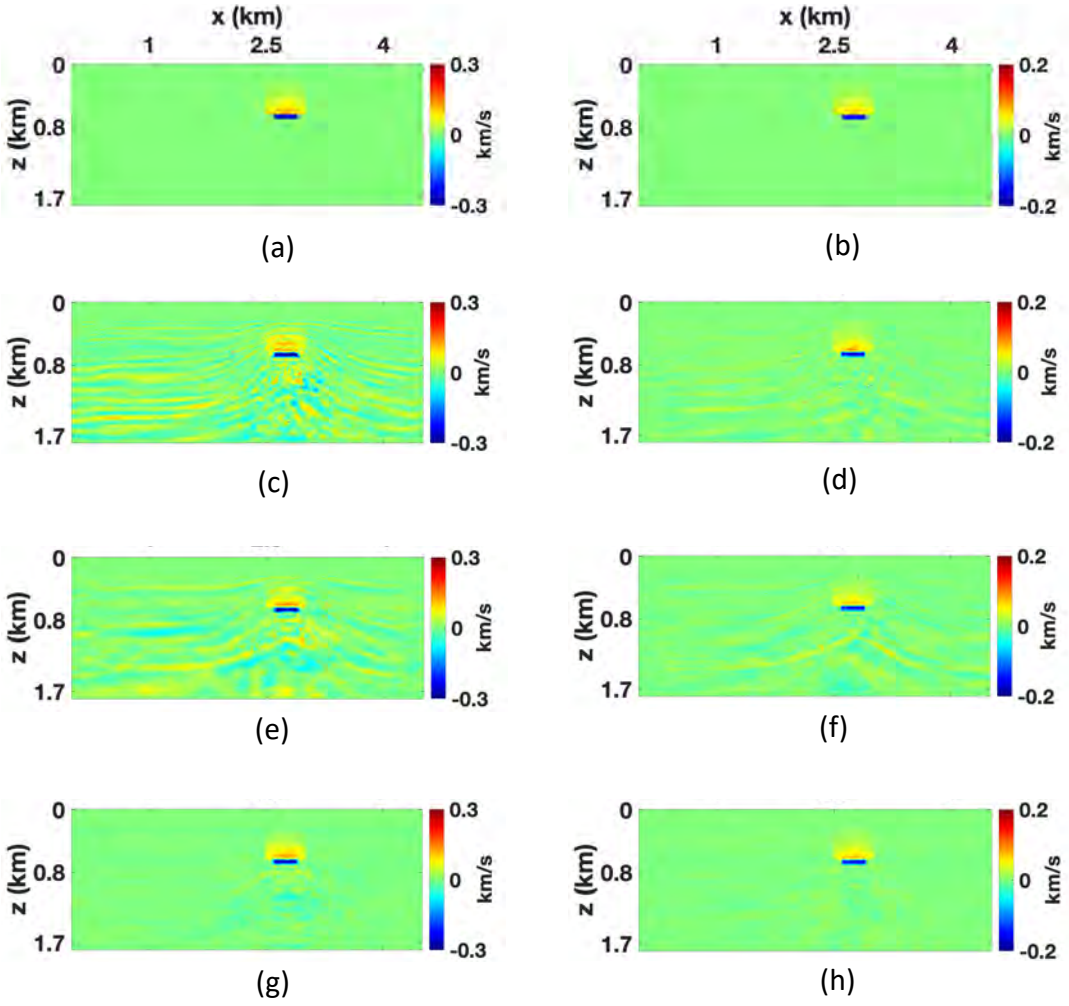

Figure 13. Time-lapse parameter variations estimated from the data with overburden changes. The actual time-lapse variations in (a) $V_{\rm P0}$ and (b) $V_{\rm S0}$. The parallel-difference strategy: (c) $V_{\rm P0}$ and (d) $V_{\rm S0}$. The sequential-difference strategy: (e) $V_{\rm P0}$ and (f) $V_{\rm S0}$. The double-difference strategy: (g) $V_{\rm P0}$ and (h) $V_{\rm S0}$.

$$\rho\frac{\partial v_z}{\partial t} = \frac{\partial \sigma_{xz}}{\partial x} + \frac{\partial \sigma_{zz}}{\partial z} + f_z, \tag{A-2}$$

where $\mathbf{v}$ is the particle velocity, and $\boldsymbol{\sigma}$ is the stress tensor. The Hooke' law for this model takes the form:

$$\frac{\partial \sigma_{xx}}{\partial t} = d_{11}\frac{\partial v_x}{\partial x} + d_{13}\frac{\partial v_z}{\partial z} + d_{15}(\frac{\partial v_x}{\partial z} + \frac{\partial v_z}{\partial x}), \tag{A-3}$$

$$\frac{\partial \sigma_{zz}}{\partial t} = d_{13}\frac{\partial v_x}{\partial x} + d_{33}\frac{\partial v_z}{\partial z} + d_{35}(\frac{\partial v_x}{\partial z} + \frac{\partial v_z}{\partial x}), \tag{A-4}$$

$$\frac{\partial \sigma_{xz}}{\partial t} = d_{15}\frac{\partial v_x}{\partial x} + d_{35}\frac{\partial v_z}{\partial z} + d_{55}(\frac{\partial v_x}{\partial z} + \frac{\partial v_z}{\partial x}), \tag{A-5}$$

where d_{11}, d_{13}, d_{15}, d_{33}, d_{35}, and d_{55} denote the stiffness coefficients given by:

$$d_{11} = (c_{11}\cos^2\theta + c_{11}\sin^2\theta)\cos^2\theta + (c_{13}\cos^2\theta + c_{33}\sin^2\theta)\sin^2\theta + 4c_{44}\cos^2\theta\sin^2\theta, \tag{A-6}$$

$$d_{13} = c_{11}\cos^2\theta\sin^2\theta + c_{13}\sin^4\theta + c_{13}\cos^4\theta + c_{33}\cos^2\theta\sin^2\theta - 4c_{44}\cos^2\theta\sin^2\theta, \tag{A-7}$$

$$d_{15} = (c_{13} - c_{11})\cos^3\theta\sin\theta + (c_{33} - c_{13})\cos\theta\sin^3\theta + 2c_{44}\cos\theta\sin\theta(\cos^2\theta - \sin^2\theta), \tag{A-8}$$

$$d_{33} = (c_{11}\sin^2\theta + c_{13}\cos^2\theta)\sin^2\theta + (c_{33}\cos^2\theta + c_{13}\sin^2\theta)\cos^2\theta + 4c_{44}\cos^2\theta\sin^2\theta, \tag{A-9}$$

$$d_{35} = (c_{13} - c_{11})\cos\theta\sin^3\theta + (c_{33} - c_{13})\cos^3\theta\sin\theta - 2c_{44}\cos\theta\sin\theta(\cos^2\theta - \sin^2\theta), \tag{A-10}$$

$$d_{55} = c_{44}(1 - 2\sin^2\theta)^2 + (c_{33} - c_{13})\cos^2\theta\sin^2\theta - (c_{13} - c_{11})\cos^2\theta\sin^2\theta, \tag{A-11}$$

where θ is the angle between the symmetry axis and the vertical, and c_{ij} is the stiffness tensor of the corresponding VTI medium. Equations A-6 to A-11 are obtained using the Bond (1943) transformation.

When $\theta = 90^\circ$, the medium becomes HTI (TI with a horizontal symmetry axis). Zero tilt ($\theta = 0^\circ$) corresponds to the VTI model, for which equations A-1 to A-5 reduce to:

$$\rho\frac{\partial v_x}{\partial t} = \frac{\partial \sigma_{xx}}{\partial x} + \frac{\partial \sigma_{xz}}{\partial z} + f_x, \tag{A-12}$$

$$\rho\frac{\partial v_z}{\partial t} = \frac{\partial \sigma_{xz}}{\partial x} + \frac{\partial \sigma_{zz}}{\partial z} + f_z, \tag{A-13}$$

$$\frac{\partial \sigma_{xx}}{\partial t} = c_{11}\frac{\partial v_x}{\partial x} + c_{13}\frac{\partial v_z}{\partial z}, \tag{A-14}$$

$$\frac{\partial \sigma_{zz}}{\partial t} = c_{13}\frac{\partial v_x}{\partial x} + c_{33}\frac{\partial v_z}{\partial z}, \tag{A-15}$$

$$\frac{\partial \sigma_{xz}}{\partial t} = c_{44}(\frac{\partial v_x}{\partial x} + \frac{\partial v_z}{\partial z}). \tag{A-16}$$

REFERENCES

Alkhalifah, T., and R. É. Plessix, 2014, A recipe for practical full-waveform inversion in anisotropic media: An analytical parameter resolution study: Geophysics, **79**, no. 3, R91–R101.

Asnaashari, A., R. Brossier, S. Garambois, F. Audebert, P. Thore, and J. Virieux, 2012, Time-lapse imaging using regularized FWI: a robustness study: SEG Technical Program Expanded Abstracts, 1–5.

———, 2013, Regularized seismic full waveform inversion with prior model information: Geophysics, **78**, no. 2, 1–49.

———, 2015, Time-lapse seismic imaging using regularized full-waveform inversion with a prior model: Which strategy?: Geophysical Prospecting, **63**, 78–98.

Bai, T., and I. Tsvankin, 2019, Source-independent waveform inversion for attenuation estimation in anisotropic media: Geophysical Prospecting, **67**, 2343–2357.

Behera, L., and I. Tsvankin, 2009, Migration velocity analysis for tilted transversely isotropic media: Geophysical Prospecting, **57**, 13–26.

Bond, W. L., 1943, The mathematics of the physical properties of crystals: The Bell System Technical Journal, **22**, 1–72.

Borges, F., M. Muzzette, L. E. Queiroz, B. Pereira-Dias, R. Dias, and A. Bulcão, 2022, Analysis of water velocity changes in time-lapse ocean bottom acquisitions - a synthetic 2d study in santos basin, offshore brazil: Journal of Applied Geophysics, **197**, 104521.

Choi, Y., and T. Alkhalifah, 2011, Source-independent time-domain waveform inversion using convolved wavefields: Application to the encoded multisource waveform inversion: Geophysics, **76**, no. 5, R125–R134.

Davy, R. G., L. Frahm, R. Bell, R. Arai, D. H. N. Barker, S. Henrys, N. Bangs, J. Morgan, and M. Warner, 2021, Generating high-fidelity reflection images directly from full-waveform inversion: Hikurangi subduction zone case study: Geophysical Research Letters, **48**, e2021GL094981.

Denli, H., and L. Huang, 2009, Double-difference elastic waveform tomography in the time domain: SEG Technical Program Expanded Abstracts, 2302–2306.

Holt, R., A. Bauer, and A. Bakk, 2016, The importance of overburden stress path in assessment of stress dependence for 4D applications: European Association of Geoscientists & Engineers, 1–5.

Kamath, N., and I. Tsvankin, 2016, Elastic full-waveform inversion for VTI media: Methodology and sensitivity analysis: Geophysics, **81**, no. 2, C53–C68.

Lecerf, D., M. Lange, A. Oates, and J. Kumar, 2022, Water column corrections: Joint water velocity inversion for 4d marine surveys: Second International Meeting for Applied Geoscience & Energy, 3404–3408.

Li, N., Z. Yu, R. To, M. Wang, Y. Xie, and D. Dickinson, 2021a, 4D FWI using towed-streamer data: A case study near Laverda oil field: SEG Technical Program Expanded Abstracts, 622–626.

Li, Y., T. Alkhalifah, and Q. Guo, 2021b, Target-oriented time-lapse waveform inversion using deep learning-assisted regularization: Geophysics, **86**, no. 4, R485–R495.

Liu, Y., and I. Tsvankin, 2021, Methodology of time-lapse elastic full-waveform inversion for VTI media: Journal of Seismic Exploration, **30**, 257–270.

———, 2022, Source-independent time-lapse full-waveform inversion for anisotropic media: Geophysics, **87**, R111–R122.

Lumley, D., 2010, 4D seismic monitoring of CO_2 sequestration: The Leading Edge, **29**, no. 2, 150–155.

Lumley, D. E., 2001, Time-lapse seismic reservoir monitoring: Geophysics, **66**, 50–53.

Luo, C. M., S. X. Wang, and S. Y. Yuan, 2014, Effect of inaccurate wavelet phase on prestack waveform inversion: Journal of Applied Geophysics, **11**, 479–488.

Pevzner, R., M. Urosevic, D. Popik, V. Shulakova, K. Tertyshnikov, E. Caspari, J. Correa, T. Dance, A. Kepic, S. Glubokovskikh, S. Ziramov, B. Gurevich, R. Singh, M. Raab, M. Watson, T. Daley, M. Robertson, and B. Freifeld, 2017, 4D surface seismic tracks small supercritical CO2 injection into the subsurface: CO2CRC Otway Project: International Journal of Greenhouse Gas Control, **63**, 150–157.

Plessix, R.-E., S. Michelet, H. Rynja, H. Kuehl, C. Perkins, J. Maag, and P. Hatchell, 2010, Some 3D applications of full waveform inversion: EAGE Expanded Abstracts.

Pratt, R. G., 1999, Seismic waveform inversion in the frequency domain, part 1: Theory and verification in a physical scale model: Geophysics, **64**, 888–901.

Routh, P., G. Palacharla, I. Chikichev, and S. Lazaratos, 2012, Full wavefield inversion of time-lapse data for improved imaging and reservoir characterization: SEG Technical Program Expanded Abstracts, 1–6.

Rusmanugroho, H., R. Modrak, and J. Tromp, 2017, Anisotropic full-waveform inversion with tilt-angle recovery: Geophysics, **82**, R135–R151.

Singh, S., and I. Tsvankin, 2020, Sensitivity analysis of FWI for elastic orthorhombic media: SEG Technical Program Expanded Abstracts, 171–175.

Singh, S., I. Tsvankin, and E. Z. Naeini, 2018, Bayesian framework for elastic full-waveform inversion with facies information: The Leading Edge, **37**, 924–931.

———, 2021, Facies-based full-waveform inversion for anisotropic media: a north sea case study: Geophysical Prospecting, **69**, 1650–1663.

Smith, S., and I. Tsvankin, 2012, Coupled geomechanical and seismic modeling of compaction-induced traveltime shifts for multi-component data: Geophysics, **77**, no. 6, 1687–1692.

Smith, S. S., and I. Tsvankin, 2013, Sensitivity of compaction-induced multicomponent seismic time shifts to variations in reservoir properties: Geophysics, **78**, no. 5, T151–T163.

Song, Z., P. R. Williamson, and R. G. Pratt, 1995, Frequency-domain acoustic-wave modeling and inversion of crosshole data: Part ii—inversion method, synthetic experiments and real-data results: Geophysics, **60**, 796–809.

Tarantola, A., 1984, Linearized inversion of seismic reflection data: Geophysical Prospecting, **32**, 998–1015.

Tsvankin, I., 2012, Seismic signatures and analysis of reflection data in anisotropic media, third edition: Society of Exploration Geophysicists.

Vigh, D., K. Jiao, D. Watts, and D. Sun, 2014, Elastic full-waveform inversion application using multicomponent measurements of seismic data collection: Geophysics, **79**, no. 2, R63–R77.

Waldhauser, F., and W. Ellsworth, 2020, A double-difference earthquake location algorithm: Method and application to the northern hayward fault, california: Bulletin of the Seismological Society of America, **90**, no. 6, 1353–1368.

Wang, X., and I. Tsvankin, 2013, Multiparameter tti tomography of p-wave reflection and vsp data: Geophysics, **78**, WC51–WC63.

Warner, M., A. Ratcliffe, T. Nangoo, J. Morgan, A. Umpleby, N. Shah, V. Vinje, I. Štekl, L. Guasch, C. Win, G. Conroy, and A. Bertrand, 2013, Anisotropic 3d full-waveform inversion: Geophysics, **78**, no. 2, R59–R80.

Watanabe, T., S. Shimizu, E. Asakawa, and T. Matsuoka, 2004, Differential waveform tomography for time-lapse crosswell seismic data with application to gas hydrate production monitoring: SEG Technical Program Expanded Abstracts, 2323–2326.

Yuan, F., S. Wang, S. Yuan, J. Wang, J. Li, P. Shi, and Y. Liu, 2014, Influence of inaccurate wavelet amplitude on frequency-domain full waveform inversion: EAGE Conference Expanded Abstracts, 1–5.

Zhang, Q., H. Zhou, Q. Li, H. Chen, and J. Wang, 2016, Robust source-independent elastic full-waveform inversion in the time domain: Geophysics, **81**, no. 2, R29–R44.

Zhang, Z., and T. Alkhalifah, 2020, High-resolution reservoir characterization using deep learning-aided elastic full-waveform inversion: The north sea field data example: Geophysics, **85**, no. 4, WA137–WA146.

Zhang, Z., T. Alkhalifah, E. Z. Naeini, and B. Sun, 2018, Multiparameter elastic full waveform inversion with facies-based con-

straints: Geophysical Journal International, **213**, no. 3, 2112–2127.

Zhou, W., and D. Lumley, 2021a, Central-difference time-lapse 4d seismic full-waveform inversion: GEOPHYSICS, **86**, R161–R172.

———, 2021b, Nonrepeatability effects on time-lapse 4D seismic full-waveform inversion for ocean-bottom node data: Geophysics, **86**, R547–R561.